

## JGR Solid Earth

## RESEARCH ARTICLE

10.1029/2019JB018813

## Pressure Dependence of Proton Incorporation and Water Solubility in Olivine

HPSTAR  
1100-2020Hongzhan Fei<sup>1</sup> and Tomoo Katsura<sup>1,2</sup><sup>1</sup>Bayerisches Geoinstitut, University of Bayreuth, Bayreuth, Germany, <sup>2</sup>Center for High Pressure Science and Technology Advanced Research, Beijing, China

## Key Points:

- Mg/Si atomic ratio in forsterite increases with increasing water content
- Protons in olivine are primarily stored in Si sites in the upper mantle, Mg=2H substitution is significant only at relatively low pressure
- Pressure dependence of water solubility in olivine is SiO<sub>2</sub>-activity dependent

## Correspondence to:

H. Fei,  
hongzhan.fe@uni-bayreuth.de

## Citation:

Fei, H., & Katsura, T. (2020). Pressure dependence of proton incorporation and water solubility in olivine. *Journal of Geophysical Research: Solid Earth*, 125, e2019JB018813. <https://doi.org/10.1029/2019JB018813>

Received 30 SEP 2019

Accepted 10 JAN 2020

Accepted article online 14 JAN 2020

**Abstract** Hydrous forsterite single crystals were synthesized at 8 GPa and 1250 °C using a multianvil apparatus under various SiO<sub>2</sub> activity conditions. Electron microprobe and transmission Fourier-transform infrared spectroscopy analyses show that the Mg/Si atomic ratio increases with increasing water content. This provides new evidence that protons are mainly stored in Si sites in hydrous forsterite. The contribution of Mg sites for proton incorporation can be significant at  $\leq 2.5$  GPa with excess SiO<sub>2</sub> but is negligible at higher pressures. Protons in olivine under asthenospheric conditions are therefore mostly maintained in Si sites. A summary of experimental studies suggests that the water solubility of forsterite/olivine equilibrated with excess (Mg,Fe)O is substantially higher than that with excess SiO<sub>2</sub>; however, this difference decreases with increasing pressure and becomes identical at 12–14 GPa. Owing to the low water solubility of olivine under topmost asthenospheric conditions, the geophysically observed low viscosity and low seismic velocity zones cannot be caused by olivine hydration, and the high conductivity anomaly should not be attributed to free H<sup>+</sup>-controlled proton conduction in olivine.

## 1. Introduction

Olivine is the most abundant minerals in the Earth's upper mantle and can incorporate 10<sup>2</sup>–10<sup>3</sup> wt. ppm water in its crystal structure as protons (Bali et al., 2008; Ferot & Bolfan-Casanova, 2012; Kohlstedt et al., 1996; Smyth et al., 2006). Even such small amounts of water may dramatically affect olivine's physical and chemical properties such as defect chemistry, atomic diffusivity, rheology, fabric transition, and melting (e.g., Costa & Chakraborty, 2008; Fei et al., 2013, 2018; Jung & Karato, 2001; Tenner et al., 2012), and can therefore alter geochemical and geophysical processes occurring in the Earth's mantle.

Protons are incorporated into olivine crystal structures in either Mg sites (Mg and Fe sites in Fe-bearing olivine) or Si sites (e.g., Beran & Putnis, 1983; Brodholt & Refson, 2000). Because different incorporation mechanisms may influence olivine properties in different ways, understanding the incorporation mechanisms is essential for investigating dynamics and geochemical circulation in the upper mantle. However, the question regarding which site dominates for proton incorporation in olivine remains unsolved and has been the subject of debate for decades. High-pressure experiments indicate that water solubility in olivine is nearly proportional to the water fugacity of the system (Bai & Kohlstedt, 1992; Bali et al., 2008; Kohlstedt et al., 1996), which suggests that protons mainly occupy Mg sites by the reaction



Additionally, first-principle calculations of point defect free energy show that the (2H)<sub>Mg</sub><sup>x</sup> is more stable than (4H)<sub>Si</sub><sup>x</sup> under pressure and temperature conditions corresponding to the upper mantle (Qin et al., 2018) (with Kröger and Vink, 1956, notation for defect chemistry). By introducing protons into an ideal forsterite crystal, V<sub>Mg</sub><sup>''</sup> sites (and/or interstitial sites) are considered to be most energetically favorable (intrinsic regime in Verma & Karki, 2009). Meanwhile, the formation of defects on Si sites is considerably more difficult than Mg sites judging from the extremely slow self-diffusivity of Si compared with Mg (e.g., Chakraborty et al., 1994; Costa and Chakraborty et al., 2008; Fei et al., 2012, 2013, 2018). All of these arguments support that Mg sites are more favorable for proton incorporation in olivine.

In contrast, theoretical simulations of infrared spectroscopy show that OH bonding related to Si sites should have absorption in the high wavenumber region (~3,450–3,600 cm<sup>-1</sup>), whereas OH related to Mg sites should have lower wavenumber absorption (~3,150–3,250 cm<sup>-1</sup>) (e.g., Balan et al., 2011; Crépeisson et al.,

2014; Ingrin et al., 2013; Umemoto et al., 2011). Because the infrared absorption peaks at 3,450–3,600  $\text{cm}^{-1}$  usually dominate the olivine spectra (e.g., Bali et al., 2008; Kohlstedt et al., 1996; Smyth et al., 2006), the majority of protons in olivine should be stored in Si sites. Specially, the main proton components are attributed to Si sites substituted by four protons from nuclear magnetic resonance spectroscopy and first-principle calculation (Xue et al., 2017) by the following the reaction:



where  $\text{SiO}_2$  and  $\text{Mg}_2\text{SiO}_4$  may further form enstatite.

Some previous studies (e.g., Berry et al., 2005; Lemaire et al., 2004; Matveev et al., 2001; Withers & Hirschmann, 2008) have investigated the effect of silica activity on the infrared spectra of olivine synthesized at 1.5–2.0 GPa and showed that absorption at 3,450–3,600  $\text{cm}^{-1}$  dominates when the Mg/Si atomic ratio in the starting material is 2.0 or higher. However, the broad peak at 3,150–3,250  $\text{cm}^{-1}$  (Fe-free forsterite) or 3,250–3,350  $\text{cm}^{-1}$  (Fe-bearing olivine) is very strong especially along the [001] axis at a Mg/Si ratio <2. Nevertheless, more recent studies at higher pressures (Bali et al., 2008; Ferot & Bolfan-Casanova, 2012; Smyth et al., 2006) do not show the strong absorption at 3,150–3,350  $\text{cm}^{-1}$  even if olivine/forsterite coexist with pyroxene/enstatite. More essentially, the water solubility in olivine is found to be sensitive to silica activity at 2–4 GPa (Matveev et al., 2001), but not at 12 GPa (Smyth et al., 2006). These experimental results lead to an inconsistent interpretation about the proton incorporation mechanism in olivine.

Measurements of the Mg/Si atomic ratio as a function of water content ( $C_{\text{H}_2\text{O}}$ ) and comparison with the ideal chemical formula can provide constraints for understanding proton substitution mechanisms in minerals. For example, the Mg/Si ratio is 2.0 in dry wadsleyite and systematically decreases with increasing  $C_{\text{H}_2\text{O}}$ ; protons are therefore primarily stored in Mg sites in wadsleyite (Demouchy et al., 2005). In contrast, Mg/Si is less sensitive to  $C_{\text{H}_2\text{O}}$  in ringwoodite and protons should therefore be stored in both Mg and Si sites (Fei & Katsura, 2020; Ohtani et al., 2000). In the case of olivine, however, owing to the much lower water solubility in comparison with wadsleyite and ringwoodite (e.g., Bali et al., 2008; Kohlstedt et al., 1996), the deviation of Mg/Si ratio from the ideal formula is very small even when saturated with water and conclusive results are thus difficult to obtain.

In this study, we synthesized hydrous olivine crystals at 8 GPa and 1250 °C and carefully compare the Mg/Si ratio in dry and hydrous olivine by electron microprobe. Combined with infrared spectroscopy analysis, our results demonstrate that Mg/Si increases with increasing water content, therefore, suggesting that protons in olivine are mostly stored in Si sites.

## 2. Experimental Procedure

### 2.1. Starting Material and Sample Capsulation

Because iron introduces additional uncertainty owing to its changeable valence, Fe-free  $\text{Mg}_2\text{SiO}_4$ -forsterite samples were used in this study. Both dry synthetic forsterite single crystal from OXIDE Co. (Mukawa, Japan) and mixtures of MgO,  $\text{SiO}_2$ , and Mg  $(\text{OH})_2$  powders (>99.9% purity) from Sigma-Aldrich Co. (Darmstadt, Germany) were used as starting materials. The chemical composition of the single crystal was characterized by laser-ablation ICP-MS, which shows a major impurity of Ir (~80 wt. ppm) and other trace elements (Mn, Ni, Fe, Al, Sc, Cr, Cu, Zn, Ga, Lu, Re, and Au) with less than 3 wt. ppm each (Fei et al., 2012). Disks with a 1.3-mm diameter cored from the single crystal were used in the following procedure. For the powder samples, MgO and  $\text{SiO}_2$  were dried at 1000 °C in an ambient-pressure furnace, whereas Mg  $(\text{OH})_2$  was dried at 125 °C in a vacuum furnace prior to weighing. Mixtures with bulk compositions of  $\text{Mg}_{2.2}\text{SiO}_{4.2} + 15 \text{ wt.}\% \text{H}_2\text{O}$  (MgO-rich) and  $\text{Mg}_2\text{Si}_{1.1}\text{O}_{4.2} + 15 \text{ wt.}\% \text{H}_2\text{O}$  ( $\text{SiO}_2$ -rich) were made by grinding in ethanol and subsequent drying at 125 °C.

Four Pt capsules with 1.6-mm outer and 1.3-mm inner diameters were prepared. The capsules were filled with (1)  $\text{Mg}_{2.2}\text{SiO}_{4.2} + 15 \text{ wt.}\% \text{H}_2\text{O}$  (hereafter MgO-rich sample), (2)  $\text{Mg}_2\text{Si}_{1.1}\text{O}_{4.2} + 15 \text{ wt.}\% \text{H}_2\text{O}$  (hereafter  $\text{SiO}_2$ -rich sample), (3) forsterite single crystal disk +  $\text{PtO}_2 \cdot x\text{H}_2\text{O}$  (~2:1 volume ratio, hereafter Fo +  $\text{PtO}_2 \cdot x\text{H}_2\text{O}$ ), (4) forsterite single crystal disk without any additions (hereafter dry Fo), and sealed by arc welding. The lengths of the capsules were 2.0 or 4.0 mm (Figure 1).

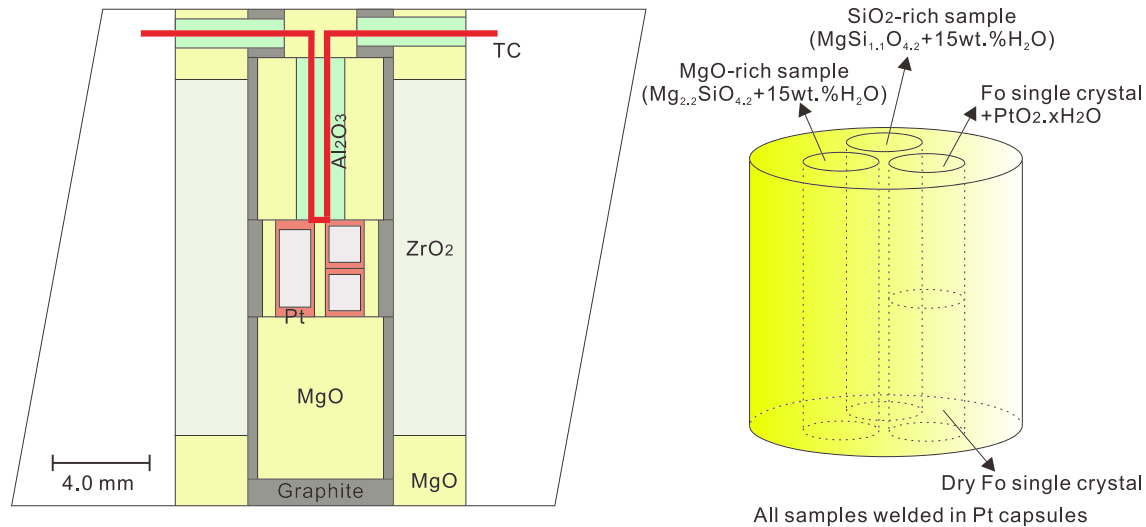


**Figure 1.** The 25/15 multianvil cell assembly with graphite furnace used in this study. Four Pt capsules with various samples were loaded within the same assembly in a single run. The lengths of MgO-rich and SiO<sub>2</sub>-rich sample capsules were 4.0 mm, and 2.0 mm for Fo + PtO<sub>2</sub>·xH<sub>2</sub>O and Dry Fo samples.

## 2.2. High-Pressure Experiment

All four capsules were inserted into an MgO chamber in a stepped graphite furnace within a ZrO<sub>2</sub> thermal insulator. A 5 wt.% Cr<sub>2</sub>O<sub>3</sub> doped MgO octahedron with edge length of 25 mm was used as pressure medium (25/15 multianvil cell assembly at the Bayerisches Geoinstitut). A W<sub>97</sub>Re<sub>3</sub>-W<sub>75</sub>Re<sub>25</sub> (D-type) thermocouple with its junction located at one end of the capsules was used to monitor the sample temperature (Figure 1). The assembly was compressed to 8 GPa in a 1,200 ton Kawai-type multianvil press using eight tungsten carbide cubes with 32-mm edge lengths and 15-mm truncated edge lengths at ambient temperature and sequentially heated to 1250 °C with a ramp heating rate of ~100 °C min<sup>-1</sup>, which is above the solidus temperature of MgO-SiO<sub>2</sub>-H<sub>2</sub>O system at 8 GPa (Bali et al., 2008; Inoue et al., 1994). After annealing at the target temperature for 6 hr, the samples were quenched by switching off the heating power supply and decompressed to ambient pressure over 10 hr.

Upon opening the capsules with small holes, water was observed to escape from the capsule, which should be exsolved from the hydrous melt when crystallized during quenching because water and silicate melt are completely miscible under the investigated conditions (Kawamoto et al., 2004; Inoue, 1994). All recovered capsules, together with a piece of additional forsterite single crystal without annealing (hereafter unannealed Fo), were mounted within the same epoxy and doubly polished to 100 μm thickness; namely, all five samples were treated identically for subsequent analyses.

## 2.3. Sample Analysis

### 2.3.1. SEM

After chemical polishing in alkaline colloidal silica solution to remove small scratches, scanning electron microscopy (SEM) analysis was performed using a backscattering detector (BSE) with an acceleration voltage of 20 kV and energy-dispersive detector (EDS) accelerated at 15 kV, and magnifications from 15X up to 1000 K X (Figure 2). The run products in the four capsules appear as forsterite + melt (MgO-rich sample), forsterite + enstatite + melt (SiO<sub>2</sub>-rich sample), forsterite + melt (Fo + PtO<sub>2</sub>·xH<sub>2</sub>O sample), and forsterite single crystal (Dry Fo sample). The grain sizes of the MgO-rich and SiO<sub>2</sub>-rich samples was 100–500 μm, whereas that of the Fo + PtO<sub>2</sub>·xH<sub>2</sub>O and dry Fo samples remain as single crystals but with some cracks, which were probably produced mechanically by compression and decompression.

### 2.3.2. Transmission FTIR Spectroscopy

Fourier-transform infrared (FTIR) spectroscopy analysis was performed on a Bruker IFS 120 high-resolution spectrometer coupled with a Bruker IR microscope. Both polarized and unpolarized infrared beams with an aperture size of 60 or 120 μm were focused on the surface and 100 or 200 scans were accumulated for each spectrum at a resolution of 2 cm<sup>-1</sup>. For the polarized FTIR analysis, spectra were collected with 90°

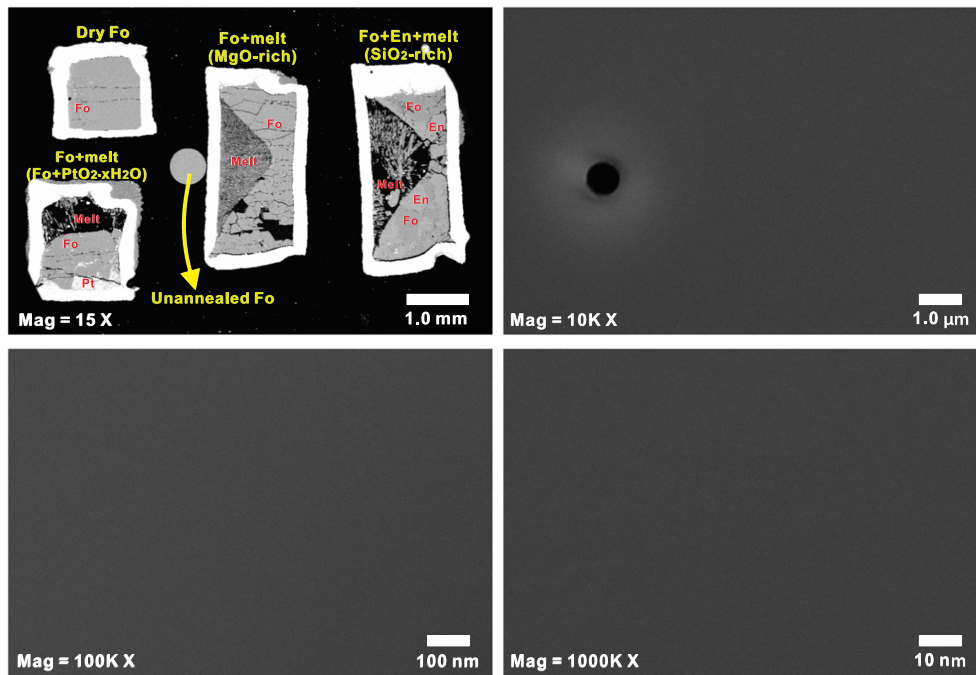


**Figure 2.** Backscattered electron images of the run products together with an unannealed forsterite crystal. (a) Low-magnification SEM image showing all the samples within epoxy. (b) High-magnification SEM image (10 K X) with a pore whose size is  $\sim 0.8 \mu\text{m}$ . (c) High-magnification (100 K X) SEM image. (d) High-magnification SEM image (1000 K X). Nanosized inclusions are not observed in the high-magnification images. Even if the inclusions were polished away during sample preparation, craters should remain on the sample surface. The images in panels (b)–(d) are from the MgO-rich sample. Nanosized inclusions are also not observed in the  $\text{SiO}_2$ -rich or Fo +  $\text{PtO}_2 \cdot x\text{H}_2\text{O}$  samples.

polarization angles on randomly orientated grains in the cross section. Seven or eight unpolarized spectra were measured for each hydrous sample on different regions within the same forsterite grain and different grains within the same capsule. Six polarized spectra were collected on three grains from each capsule. Grain boundaries and cracks were avoided in the analysis.

After baseline subtraction,  $C_{\text{H}_2\text{O}}$  was calculated by integration of each FTIR spectrum from 3,000 to 4,000  $\text{cm}^{-1}$  using the Withers et al. (2012) calibration,

$$C_{\text{H}_2\text{O}} = 3 \times 10^6 \times \int \frac{A(\nu) \cdot M_{\text{H}_2\text{O}}}{\epsilon \cdot \tau \cdot \rho} d\nu \quad (3)$$

where 3 is the unpolarized FTIR correction for three directions,  $A(\nu)$  is the infrared absorption at wavenumber  $\nu$ ,  $M_{\text{H}_2\text{O}}$  is the molar weight of water ( $18.02 \text{ g mol}^{-1}$ ),  $\epsilon$  is the infrared absorption coefficient ( $45,200 \text{ L mol}^{-1} \text{ cm}^{-2}$ , Withers et al., 2012),  $\tau$  is sample thickness, and  $\rho$  is the density of forsterite ( $3,300 \text{ g L}^{-1}$ ). Bulk  $C_{\text{H}_2\text{O}}$  of the polarized analysis was obtained by equation (3) with the third direction from the average of the two analyzed polarization directions. If using the older calibration by Bell et al. (2003), the  $C_{\text{H}_2\text{O}}$  would be higher by a factor of  $\sim 1.58$  owing to the lower  $\epsilon$  ( $28,450 \text{ L mol}^{-1} \text{ cm}^{-2}$ ).

Although polarized FTIR with crystallographic orientations may provide more precise  $C_{\text{H}_2\text{O}}$  results, the number of grains that can be measured is limited owing to the grain size requirement for polishing along three crystallographic orientations. This also prohibits any further microstructural observations of the whole capsule. Nevertheless, our unpolarized and polarized FTIR analysis on various crystals with random orientations demonstrate that both the spectra shape and calculated  $C_{\text{H}_2\text{O}}$  are highly reproducible (Table 1).

### 2.3.3. EPMA

MgO and  $\text{SiO}_2$  components in the samples were analyzed using a JOEL JXA-8200 microprobe with a wavelength-dispersive spectrometer operated with an acceleration voltage of 15 kV and beam current of 15 nA. The unannealed Fo sample was used for standard calibration. The counting time for each point analysis was 30 s. To avoid systematic measurement errors, the five samples were analyzed sequentially, i.e., five

**Table 1**  
Summary of Sample Analysis by FTIR, EPMA, and SEM

Sample	Starting material	Run product	Mg/Si in Fo (by EPMA)	Mg/Si in melt (by SEM-EDS)	C <sub>H2O</sub> (unpolarized FTIR, wt. ppm)	C <sub>H2O</sub> (polarized FTIR, wt. ppm)
Unannealed Fo	Fo single crystal	—	2.000 (7) <sup>a</sup>	—	<1	<1
Dry Fo	Fo single crystal	Fo	1.999 (7)	—	<1	<1
MgO-rich	Mg <sub>2.2</sub> SiO <sub>4.2</sub> + 15wt.%H <sub>2</sub> O	Fo + melt	2.044 (11)	5.59 (28)	2,800 (300)	3,000 (500)
SiO <sub>2</sub> -rich	Mg <sub>2</sub> Si <sub>1.1</sub> O <sub>4.2</sub> + 15wt.%H <sub>2</sub> O	Fo + En + melt	2.010 (9)	1.21 (3)	530 (60)	540 (30)
Fo + PtO <sub>2</sub> ·xH <sub>2</sub> O	Fo single crystal + PtO <sub>2</sub> ·xH <sub>2</sub> O	Fo + melt	2.006 (9)	1.43 (8)	540 (50)	580 (40)

Note. Note that C<sub>H2O</sub> is calculated based on the Withers et al. (2012) calibration. With the calibration of Bell et al. (2003), C<sub>H2O</sub> values would be higher by a factor of ~1.58. Error bars represent one standard deviation of the EPMA and FTIR analyses. Fo = forsterite; En = enstatite; Melt = quenched crystallized melt.  
<sup>a</sup>The unannealed Fo sample was used as a standard for EPMA analysis by assuming it as ideal Mg<sub>2</sub>SiO<sub>4</sub> forsterite with Mg/Si = 2.

points were analyzed on each sample, 25 points for the five samples in one cycle, for a total of 10 cycles of measurements. Standard calibration factors were corrected in each cycle. To prevent any biases, no data points of the Electron probe micro-analyzer (EPMA) analysis were discarded.

### 3. Experimental Results

#### 3.1. Infrared Spectra and C<sub>H2O</sub> by FTIR

To provide the most reliable comparisons of FTIR spectra shapes from different samples, the initial data without any baseline correction and thickness normalization are shown in Figure 3, although such corrections are required to calculate C<sub>H2O</sub>. None of the spectra show broad bands at ~3,400 cm<sup>-1</sup>, namely, the effects of inclusions and fluid phases on C<sub>H2O</sub> calculation are negligible. The dry Fo and unannealed Fo samples do not show any identifiable infrared absorption, indicating extremely low C<sub>H2O</sub> because even 1–3 wt. ppm of water in forsterite is clearly detectable by our FTIR facility (e.g., Demouchy & Mackwell, 2003).

All the hydrous-condition samples (MgO-rich, SiO<sub>2</sub>-rich, and Fo + PtO<sub>2</sub>·xH<sub>2</sub>O) show major absorption peaks at wavenumbers of 3,612, 3,577, 3,564, 3,548, 3,533, and 3,477 cm<sup>-1</sup>, as comparable with previously studies of both Fe-free forsterite and natural Fe-bearing olivine (e.g., Bali et al., 2008; Demouchy &

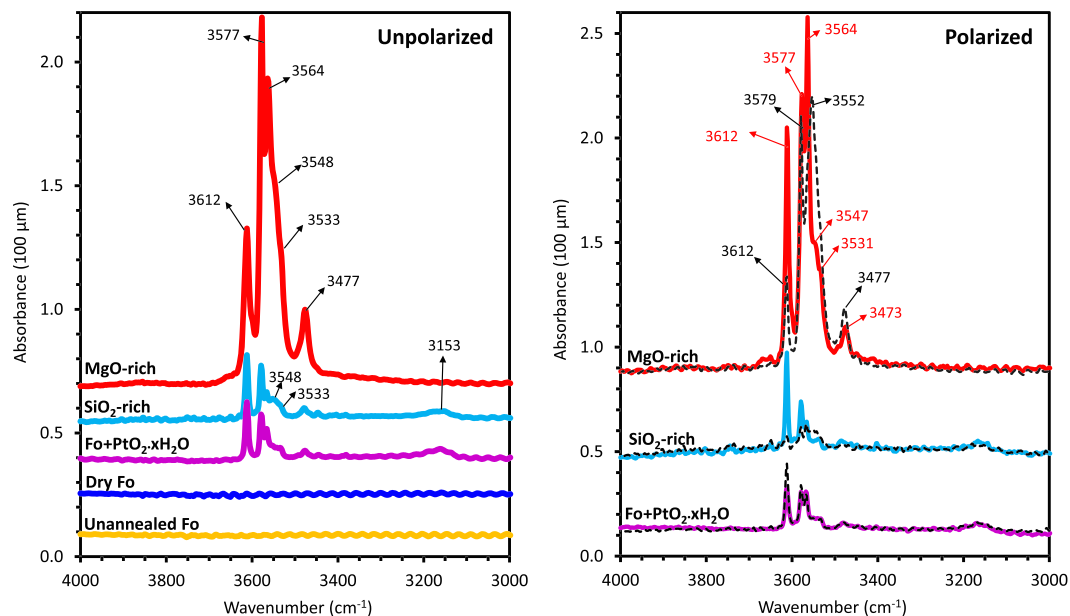


**Figure 3.** Initial FTIR spectra data of the five samples with 100 μm thickness. No baseline correction or thickness normalization have been performed in this figure. The spectra are vertically shifted for visibility. The absence of broad bands at ~3,400 cm<sup>-1</sup> indicates that effects of inclusions or fluid phases on the estimation of C<sub>H2O</sub> in forsterite are negligible. (a) With unpolarized light. (b) With polarized light on randomly oriented grains. The solid and dashed lines for each sample indicate spectra collected on the same grain but with 0 and 90 degree polarization, respectively.

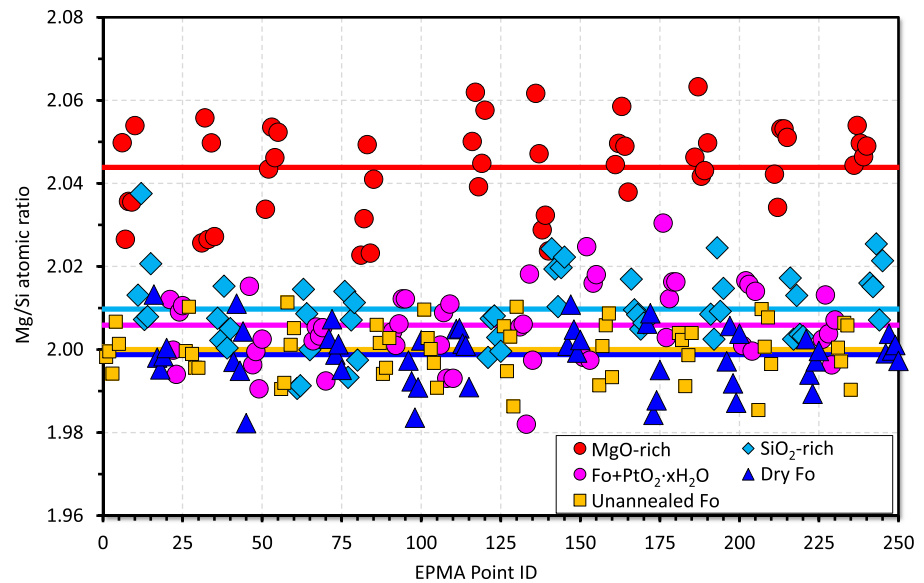


**Figure 4.** Mg/Si atomic ratios in the samples measured by EPMA. Although the data points are largely scattered owing to the EPMA resolution, the MgO-rich sample has clearly higher Mg/Si ratios than the other samples.

Mackwell, 2006; Ferot & Bolfan-Casanova, 2012; Smyth et al., 2006). The total absorption of the MgO-rich sample is  $\sim 5$  times higher than that of the SiO<sub>2</sub>-rich sample. Thus,  $C_{\text{H}_2\text{O}}$  in the MgO-rich sample is also  $\sim 5$  times higher (2,800–3,000 vs. 530–540 wt. ppm based on the calibration of Withers et al., 2012; or 4,600 vs. 800 wt. ppm based on the FTIR calibration of Bell et al., 2003) (Table 1). More Si vacancies should be produced under MgO-rich conditions than SiO<sub>2</sub>-rich conditions. The higher water content in MgO-rich sample therefore indicates that protons are mostly incorporated in Si sites.

The spectra of the SiO<sub>2</sub>-rich sample show a small broad peak at 3,153 cm<sup>-1</sup>. However, such a small peak does not appear in the MgO-rich sample. The absorption at 3,153 cm<sup>-1</sup> may therefore correspond to OH bonding related to Mg sites. Even when buffered with enstatite, the majority of absorption is still located at 3,450–3,600 cm<sup>-1</sup>. It differs from Bali et al. (2008) and Lemaire et al. (2004) who showed very strong absorption at 3,150–3,250 cm<sup>-1</sup> under high SiO<sub>2</sub>-activity conditions at  $\leq 2.5$  GPa. This low wavenumber band, namely, Mg-site related protons, thus becomes less significant with increasing pressure (Bali et al., 2008; Xue et al., 2017).

The Fo + PtO<sub>2</sub>·xH<sub>2</sub>O sample shows an identical spectrum to the SiO<sub>2</sub>-rich sample with a small peak at 3,153 cm<sup>-1</sup>. This is understandable if protons primarily substitute at Si sites because the melt in the Fo + PtO<sub>2</sub>·xH<sub>2</sub>O sample capsule becomes SiO<sub>2</sub> rich, as demonstrated by the melt composition (Table 1). The Fo + PtO<sub>2</sub>·xH<sub>2</sub>O sample is thus within SiO<sub>2</sub>-rich surroundings even though enstatite grains are not observed in this capsule.

Although preserving water in a small capsule is technically difficult, the lower  $C_{\text{H}_2\text{O}}$  in the SiO<sub>2</sub>-rich sample (and Fo + PtO<sub>2</sub>·xH<sub>2</sub>O sample) cannot be caused by water escape from the Pt capsule because (1) SEM images demonstrate that all capsules were ideally welded, (2) large melt proportions remain in all hydrous condition capsules, demonstrating hydrous conditions at high temperature, and (3) when three phases (forsterite + enstatite + melt) coexist in the three-component (MgO-SiO<sub>2</sub>-H<sub>2</sub>O) system, the  $C_{\text{H}_2\text{O}}$  in forsterite is fixed based on the phase rule, therefore, even if some water loss occurs during welding, it should not affect  $C_{\text{H}_2\text{O}}$  in the SiO<sub>2</sub>-rich sample.

### 3.2. Mg/Si Atomic Ratio by EPMA

All Mg/Si ratios of the 250 points measured by EPMA are plotted in Figure 4. The Mg/Si ratios of dry Fo are  $1.999 \pm 0.007$  (Table 1, where error bars represent one standard deviation of the EPMA analysis), and those of the SiO<sub>2</sub>-rich and Fo + PtO<sub>2</sub>·xH<sub>2</sub>O samples are  $2.010 \pm 0.009$  and  $2.006 \pm 0.009$ , respectively, both of which are slightly higher than those of the dry Fo and unannealed Fo samples. However, the

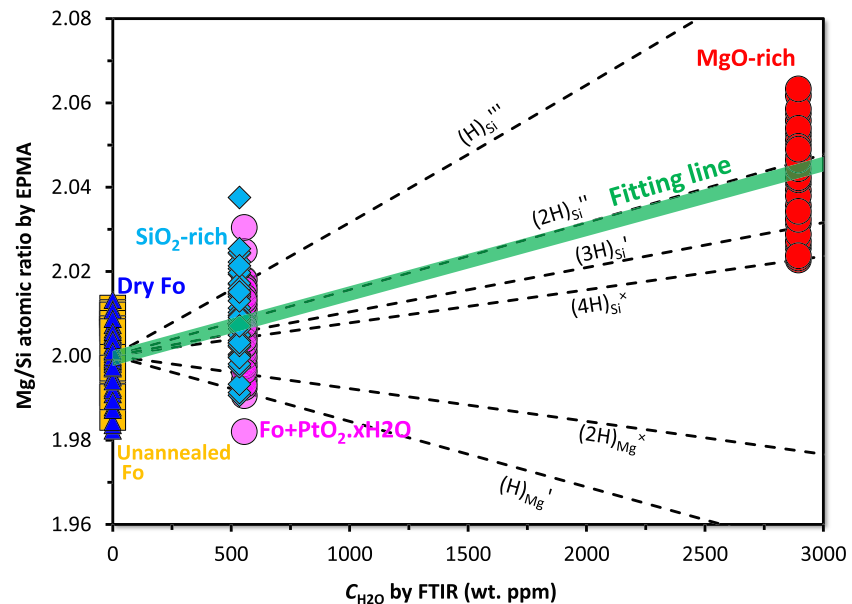


**Figure 5.** Relationship between Mg/Si atomic ratio by EPMA and  $C_{\text{H}_2\text{O}}$  by FTIR. The thick line is the linear fitting of all data points. The dashed lines are theoretical calculations of the Mg/Si ratio by assuming different incorporation mechanisms.

MgO-rich sample has  $\text{Mg/Si} = 2.044 \pm 0.011$ . Although the data points are relatively scattered owing to EPMA limitations (Figure 4), the mean values and standard deviations indicate 99.2% probability that the MgO-rich sample has a larger Mg/Si ratio than the  $\text{SiO}_2$ -rich sample calculated from the cumulative distribution function of the normal Gaussian distribution. The Mg/Si ratio can therefore be concluded to increase with increasing  $C_{\text{H}_2\text{O}}$ . This suggests that protons primarily substitute at Si sites in the crystal structure.

MgO or  $\text{Mg}(\text{OH})_2$  inclusions may cause high Mg/Si ratios; however, this should not be the case in this study for the following reasons. First, only a few  $>0.5\text{-}\mu\text{m}$  inclusions or pores are found (Figure 2b) that are large enough to be avoided in EPMA analysis, whereas 1–100 nm inclusions are absent in the high-resolution SEM observations at 10 K–1000 K X magnifications (Figures 2b–2d). Note that transmission electron microscopy is not suitable to determine the absence of inclusions because it only observes a very limited area. Second, the FTIR spectra do not show any evidence of inclusions because very broad infrared absorption at  $\sim 3,400\text{ cm}^{-1}$  should appear if there is a high concentration of nanosized inclusions. Third, if the MgO-rich sample had a low Mg/Si ratio and the apparent high Mg/Si is caused by inclusions, the data points should be scattered from  $\text{Mg/Si} = \sim 2.0$  to very high values because the analysis positions were randomly selected. Nevertheless, the values are consistently higher than 2.02 (Figure 4). Finally, to produce  $\text{Mg/Si} = \sim 2.044$  by MgO or  $\text{Mg}(\text{OH})_2$  inclusions with 1–2% volume fractions in forsterite are required, which is sufficiently high for detection by SEM. The high Mg/Si ratio in MgO-rich sample is therefore convincing.

## 4. Discussion and Implications

### 4.1. Proton Incorporation Mechanism in Forsterite/Natural Olivine

The conclusive finding of this study is that the Mg/Si atomic ratio is larger than 2.0 in hydrous forsterite (Figures 4 and 5). This provides new evidence that protons are dominantly incorporated on Si sites. Although EPMA analysis does not provide information regarding the type of proton defects in the Si sites, the slope of the fitting line is close to  $(2\text{H})_{\text{Si}}''$  substitution, whereas  $(3\text{H})_{\text{Si}}'$  and  $(4\text{H})_{\text{Si}}^{\times}$  substitutions cannot be excluded owing to EPMA uncertainties. Essentially,  $(4\text{H})_{\text{Si}}^{\times}$  substitution is charge balanced and therefore mostly preferred. Indeed, using the FTIR calibration of Bell et al. (2003), the slope of the fitting line will be smaller and consequentially closer to  $(4\text{H})_{\text{Si}}^{\times}$  substitution. Thus,  $(2\text{H})_{\text{Si}}''$ ,  $(3\text{H})_{\text{Si}}'$ , or most likely  $(4\text{H})_{\text{Si}}^{\times}$  may

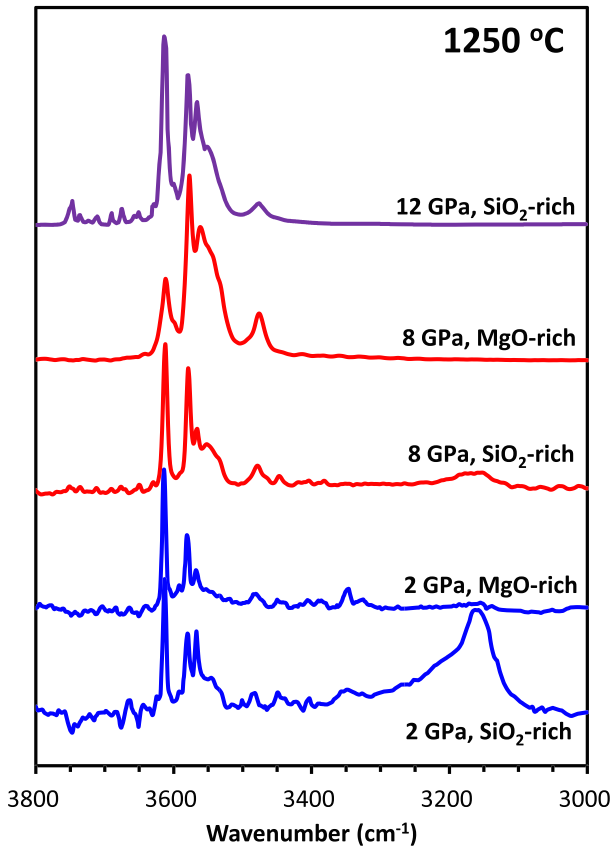


**Figure 6.** Pressure dependence of FTIR spectra in forsterite. The absorption at  $\sim 3,150\text{--}3,250\text{ cm}^{-1}$  is negligible under MgO rich conditions. Under  $\text{SiO}_2$  rich conditions, in contrast, absorption at this range is strong at relatively low pressure, and becomes less significant with increasing pressure. The 2 and 12 GPa spectra are from Lemaire et al. (2004) and Smyth et al. (2006), respectively, by summation of polarized spectra along three orientations, whereas the 8 GPa data from this study are from unpolarized FTIR analysis. All spectra are vertically expanded or squeezed for visibility.

incorporation mechanism is more preferred at higher pressure in spite of MgO-rich or  $\text{SiO}_2$ -rich conditions. In contrast, reactions (1) and (2) at relatively low pressures ( $\leq 2.5$  GPa) have a comparable free energy reduction (Brodholt & Refson, 2000). In such cases, the incorporation mechanism should be mostly controlled by the chemical environment. Namely, reaction (1) is preferred under  $\text{SiO}_2$ -rich conditions, whereas reaction (2) is preferred under MgO-rich conditions (Figure 6).

Some previous studies have argued that protons in olivine/forsterite should be dominated by  $(2\text{H})_{\text{Mg}}^{\times}$  defects because water solubility is proportional to water fugacity ( $f_{\text{H}_2\text{O}}$ ) (e.g., Bai & Kohlstedt, 1992). However, such arguments might be incorrect because the  $f_{\text{H}_2\text{O}}$  in those experiments was controlled by pressure; therefore, pressure and  $f_{\text{H}_2\text{O}}$  effects on water solubility are impossible to determine independently within a limited pressure range ( $< 0.3$  GPa). Additionally, even though  $[(4\text{H})_{\text{Si}}^{\times}]$  is proportional to  $f_{\text{H}_2\text{O}}^2$  (Table 2), the water solubility data reported at higher pressures actually fit well to  $f_{\text{H}_2\text{O}}$  exponents of either 0.5 or 2 by considering the scattering of data (Otsuka and Karato, 2011).

Olivine in the upper mantle coexists with pyroxene. Water may be primarily stored in Mg sites only at high  $\text{SiO}_2$  activity and low pressure ( $\leq 2.5$  GPa), corresponding to shallow lithosphere conditions. When natural olivine is annealed at higher pressures (e.g., Kohlstedt et al., 1996; Mosenfelder et al., 2006; Padron-Navarta & Hermann, 2017), FTIR absorptions at 3,612, 3,578, 3,564, 3,548, and 3,473  $\text{cm}^{-1}$ , which dominate in our forsterite samples, are also the major peaks in their samples with a pyroxene buffer. Because certain infrared peaks should represent the same type of defect, the majority of protons in natural olivine should be

be the major defect species for protons in forsterite, but not  $\text{H}_{\text{Mg}}'$  or  $(2\text{H})_{\text{Mg}}^{\times}$ , although they may lightly contribute under the investigated pressure and temperature conditions with excess  $\text{SiO}_2$ .

A comparison of FTIR spectra at various pressures (Figure 6, as well as Bali et al., 2008; Withers et al., 2011) shows that the contribution of Mg-site protons (absorption at  $3,150\text{--}3,250\text{ cm}^{-1}$ ) is significant under only relatively low pressure ( $\leq 2.5$  GPa) and high silica activity conditions (buffered with pyroxene). With increasing pressure, it becomes much less significant and finally negligible at 12 GPa (e.g., Bali et al., 2008; Berry et al., 2005; Lemaire et al., 2004; Padron-Navarta & Hermann, 2017; Smyth et al., 2006). In contrast, with excess MgO, the incorporation of protons in the Mg sites is always negligible. This can be explained by the volume change of the incorporation reactions described below.

For the Mg site incorporation reaction (equation (1)), the volume change,  $\Delta V_1$ , is,

$$\Delta V_1 = 2V_{\text{MgO}} + V_{(4\text{H})\text{SiO}_4} - V_{\text{Mg}_2\text{SiO}_4} - 2V_{\text{H}_2\text{O}}. \quad (4)$$

For the Si site incorporation reaction (equation (2)), by considering the formation of  $\text{MgSiO}_3$  from  $\text{Mg}_2\text{SiO}_4$  and  $\text{SiO}_2$ ,  $\Delta V_2$  becomes

$$\begin{aligned} \Delta V_2 &= V_{\text{SiO}_2} + V_{\text{Mg}_2(4\text{H})\text{O}_4} - V_{\text{Mg}_2\text{SiO}_4} - 2V_{\text{H}_2\text{O}} \\ &= 2V_{\text{MgSiO}_3} + V_{\text{Mg}_2(4\text{H})\text{O}_4} - 2V_{\text{Mg}_2\text{SiO}_4} - 2V_{\text{H}_2\text{O}}. \end{aligned} \quad (5)$$

We have  $\Delta V_1 - \Delta V_2 \approx 2V_{\text{MgO}} - 2V_{\text{MgSiO}_3} + V_{\text{Mg}_2\text{SiO}_4}$  by assuming  $V_{\text{Mg}_2(4\text{H})\text{O}_4} \approx V_{(4\text{H})\text{SiO}_4} \approx V_{\text{Mg}_2\text{SiO}_4}$ . According to the equations of state of  $\text{MgO}$ , forsterite, and orthoenstatite, we have  $V_{\text{MgO}} = 11.3 \sim 10.4\text{ cm}^3\text{ mol}^{-1}$ ,  $V_{\text{MgSiO}_3} = 31.3 \sim 28.6\text{ cm}^3\text{ mol}^{-1}$ , and  $V_{\text{Mg}_2\text{SiO}_4} \approx 43.6 \sim 40.0\text{ cm}^3\text{ mol}^{-1}$  at  $0 \sim 14$  GPa (Angel & Jackson, 2002; Dorogokupets, 2010; Finkelstein et al., 2014). Therefore,  $\Delta V_1 - \Delta V_2 = 3.5 \sim 3.8\text{ cm}^3\text{ mol}^{-1} > 0$ . This means that by incorporating the same amount of protons, the products of reaction (2) have a smaller volume than reaction (1) by  $3.5 \sim 3.8\text{ cm}^3\text{ mol}^{-1}$ . This difference would be even larger by the orthoenstatite to high-P clinoenstatite phase transformation at  $\sim 9$  GPa. Thus, the Si site

**Table 2**

Dependences of Defect Concentrations on Water Fugacity Under Various Charge Neutrality Conditions Expressed as the Exponent  $r$  in the Relationship  $[V] \propto f_{\text{H}_2\text{O}}^r$

Charge neutrality	$[(\text{OH})_{\text{O}}^{\bullet}]$	$[\text{V}_{\text{O}}^{\bullet\bullet}]$	$[\text{V}_{\text{Mg}}^{\prime\prime}]$	$[\text{H}_{\text{Mg}}^{\prime}]$	$[(2\text{H})_{\text{Mg}}^{\times}]$	$[\text{V}_{\text{Si}}^{\prime\prime\prime}]$	$[\text{H}_{\text{Si}}^{\prime\prime}]$	$[(2\text{H})_{\text{Si}}^{\prime\prime}]$	$[(3\text{H})_{\text{Si}}^{\prime}]$	$[(4\text{H})_{\text{Si}}^{\times}]$
$[(\text{OH})_{\text{O}}^{\bullet}] = 4[\text{V}_{\text{Si}}^{\prime\prime\prime}]$	2/5	-1/5	1/5	3/5	1	2/5	4/5	6/5	8/5	2
$[(\text{OH})_{\text{O}}^{\bullet}] = 3[\text{H}_{\text{Si}}^{\prime\prime\prime}]$	1/2	0	0	1/2	1	0	1/2	1	3/2	2
$[(\text{OH})_{\text{O}}^{\bullet}] = 2[(2\text{H})_{\text{Si}}^{\prime\prime\prime}]$	2/3	1/3	-1/3	1/3	1	-2/3	0	2/3	4/3	2
$[(\text{OH})_{\text{O}}^{\bullet}] = [(3\text{H})_{\text{Si}}^{\prime}]$	1	1	-1	0	1	-2	-1	0	1	2
$[\text{Fe}_{\text{Me}}^{\bullet}] = 2[\text{V}_{\text{Me}}^{\prime\prime}]$	1/2	0	0	1/2	1	0	1/2	1	3/2	2
$[(\text{OH})_{\text{O}}^{\bullet}] = 2[\text{V}_{\text{Me}}^{\prime\prime}]$	1/3	-1/3	1/3	2/3	1	2/3	1	4/3	5/3	2
$[\text{Fe}_{\text{Me}}^{\bullet}] = [\text{H}_{\text{Me}}^{\prime}]$	3/4	1/2	-1/2	1/4	1	-1	-1/4	1/2	5/4	2
$[(\text{OH})_{\text{O}}^{\bullet}] = [\text{H}_{\text{Me}}^{\prime}]$	1/2	0	0	1/2	1	0	1/2	1	3/2	2

Note. Note that  $C_{\text{H}_2\text{O}} \propto f_{\text{H}_2\text{O}}^k$ , where  $k$  depends on which type of defect dominates for proton incorporation, i.e.,  $k = 1$  and  $2$  if protons mostly form  $(2\text{H})_{\text{Mg}}^{\times}$  and  $(4\text{H})_{\text{Si}}^{\times}$ , respectively.

accommodated in Si sites in the deep asthenosphere (>2.5 GPa). The occurrence of Mg, Ti, or  $\text{Fe}^{3+}$  related proton incorporation or interstitial  $\text{OH}^-$ , corresponding to 3,150–3,250, 3,525, 3,572, and 3,350  $\text{cm}^{-1}$  absorptions (e.g., Balan et al., 2014; Berry et al., 2005; Blanchard et al., 2017) are not the dominant mechanisms. Although geologically collected natural olivine samples frequently show strong infrared absorptions at 3,150–3,350  $\text{cm}^{-1}$  (Mg- and  $\text{Fe}^{3+}$ -related protons) and relatively weak peaks at 3,450–3,600  $\text{cm}^{-1}$  (e.g., Miller et al., 1987), these could either be originally from shallow regions or represent incorporation mechanism changes induced by decreasing pressure during upwelling.

#### 4.2. Pressure Dependence of Water Solubility in Forsterite/Olivine

Silicate melt and water are completely miscible under high pressure (>3 GPa) and high temperature conditions corresponding to our experiments (Kawamoto et al., 2004; Inoue, 1994). In such cases, water solubility is generally defined as the water contents in minerals that coexist with hydrous melt (e.g., Demouchy et al., 2005; Hirschmann et al., 2005). When the melt composition changes (e.g., Mg/Si ratio), the water fugacity in the melt may also change, thus, altering the water solubility. As a result, olivine that coexists with enstatite + melt (our  $\text{SiO}_2$ -rich sample) or with only melt (our MgO rich sample) have different water contents although both are equilibrated with hydrous melt (different melt compositions). Therefore, our MgO-rich and  $\text{SiO}_2$ -rich samples, with water contents of ~3,000 and ~540 wt. ppm, should represent the water solubility of forsterite under MgO- and  $\text{SiO}_2$ -rich conditions, respectively, at the given pressure and temperature.

The water solubility in forsterite under MgO-rich conditions is about 5 times higher than that of the  $\text{SiO}_2$ -rich sample in this study. Lemaire et al. (2004) did not show a clear difference in water solubility between high and low  $\text{SiO}_2$  activity experiments, but the maximum Mg/Si ratio in their starting materials was 2.0, which is the same case as our Fo +  $\text{PtO}_2 \cdot x\text{H}_2\text{O}$  sample, thus, all of their samples were indeed under  $\text{SiO}_2$ -rich conditions. Matveev et al. (2001)'s experiments show that Fe-bearing olivine in equilibrium with ferropericlase contains 5–10 times more water than those in equilibrium with orthopyroxene at 2–4 GPa, which agrees with our results and those of Withers and Hirschmann (2008) at 8 GPa. On the other hand, Smyth et al. (2006) obtained almost identical water solubilities in forsterite under MgO- and  $\text{SiO}_2$ -rich conditions at 12 GPa. We therefore hypothesize a different pressure dependence of water solubility between MgO- and  $\text{SiO}_2$ -rich conditions.

To examine this hypothesis, we plot previously reported experimental data of water solubility in forsterite/olivine as a function of pressure in Figure 7 (This study; Bai & Kohlstedt, 1992; Bali et al., 2008; Ferot & Bolfan-Casanova, 2012; Grant, Brooker, et al., 2007; Grant, Kohn, & Brooker, 2007; Lemaire et al., 2004; Litasov et al., 2007; Matveev et al., 2001; Mosenfelder et al., 2006; Smyth et al., 2006; Withers and Hirschmann, 2008; Withers et al., 2011; Zhao et al., 2004). Because temperature has a significant effect on water solubility (Bali et al., 2008; Ferot & Bolfan-Casanova, 2012), only the literature data at temperatures of 1,200 to 1,300 °C are plotted alongside our data in Figure 7 by considering a  $\pm 50$  °C temperature uncertainty in large-volume high-pressure experiments even though data exit over a wider temperature range (e.g., Kohlstedt et al., 1996; Padron-Navarta & Hermann, 2017; Withers & Hirschmann, 2008). Additionally, because different infrared calibrations (Bell et al., 2003; Paterson, 1982; Withers et al., 2012) were adopted in these studies, all data are adjusted to the Withers et al. (2012) calibration by simply using

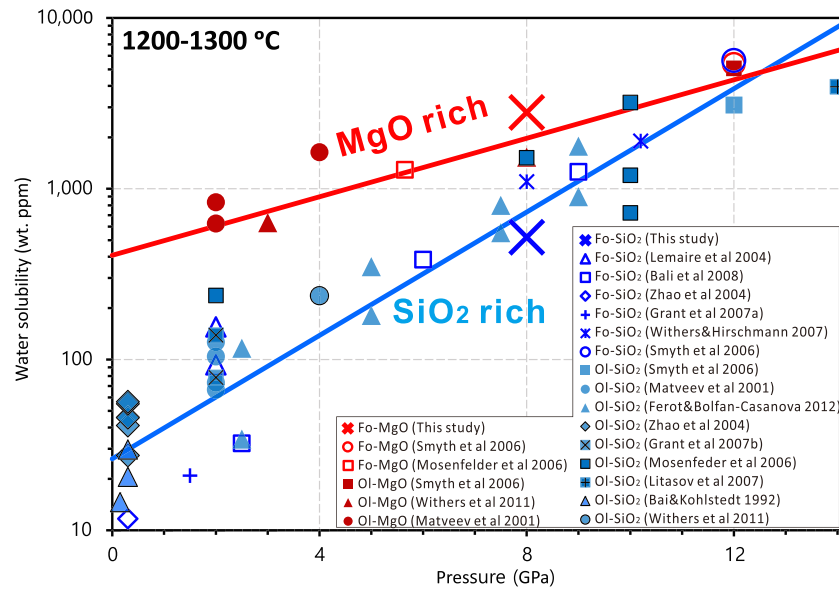


**Figure 7.** Pressure dependence of water solubility in Fe-free forsterite and Fe-bearing olivine. The blue and red symbols represent data points under  $\text{SiO}_2$ -rich and MgO-rich conditions, respectively. Only data points from previous studies that clearly mention the  $\text{SiO}_2$  or MgO buffering states (e.g., starting material rich in MgO, brucite, talc, or enstatite; with (Mg,Fe)/Si ratio; or run product coexisting with orthopyroxene or ferroperricase) are plotted. All experimental temperature conditions were 1200–1300 °C and water contents adjusted to the FTIR calibration of Withers et al. (2012). Fo-MgO: Fe-free forsterite under MgO rich conditions. Fo-SiO<sub>2</sub>: Fe-free forsterite under SiO<sub>2</sub>-rich conditions. Ol-MgO: Fe-bearing olivine under Mg (Fe)O-rich conditions. Ol-SiO<sub>2</sub>: Fe-bearing olivine under SiO<sub>2</sub>-rich conditions.

a factor of 3.5 from Paterson (1982) to Bell et al. (2003) and a factor of 0.63 from Bell et al. (2003) to Withers et al. (2012). As shown in Figure 7, the water solubility systematically increases with increasing pressure under both MgO-rich and SiO<sub>2</sub>-rich conditions. However, they follow different pressure dependences. At relatively low pressure, water solubility under MgO-rich conditions is more than one order of magnitude higher than under SiO<sub>2</sub>-rich conditions. With increasing pressure, the difference becomes smaller and finally identical at ~12–14 GPa. We perform linear least-squares fittings of the data in Figure 7 to the pressure-derivative of the Arrhenius equation at a fixed temperature of 1250 °C,

$$\Delta V = - \left( \frac{RT \partial \ln C}{\partial P} \right)_T \quad (6)$$

where  $R$  is the ideal gas constant,  $T$  is temperature,  $P$  is pressure, and  $C$  is water solubility at 1200–1300 °C, and obtain activation volumes ( $\Delta V$ ) of  $\Delta V_{\text{MgO-rich}} = -2.5 \pm 0.5$  and  $\Delta V_{\text{SiO}_2\text{-rich}} = -5.3 \pm 0.4 \text{ cm}^3 \text{ mol}^{-1}$  for MgO- and SiO<sub>2</sub>-rich conditions, respectively. These two values differ by  $\sim 3 \text{ cm}^3 \text{ mol}^{-1}$ , which is identical to  $\Delta V_1 - \Delta V_2$  as discussed previously.

The results also show that there is no clear difference of water solubility between Fe-free forsterite and Fe-bearing olivine over their entire stability fields (up to 14 GPa) under both MgO- and SiO<sub>2</sub>-rich conditions (Figure 7). Because Fe in olivine occupies Mg sites, only the hydration process on Mg sites could be affected by Fe. Water solubility is therefore insensitive to fayalite content. Zhao et al. (2004) reported a noticeable fayalite content dependence of water solubility, but their experiments were performed at 0.3 GPa, under which the contribution of Mg sites for protonation is relatively large.

### 4.3. Cation Defect Concentrations

With regards to proton storage on Si sites, all arguments based on  $(2\text{H})_{\text{Mg}}^{\times}$  substitution models should be reconsidered (e.g., Fei & Katsura, 2016; Zhao et al., 2004). Dry-condition atomic diffusion experiments suggest that the concentrations of Si vacancies ( $[\text{V}_{\text{Si}}^{\prime\prime\prime}]$ ) are substantially lower than Mg vacancies ( $[\text{V}_{\text{Mg}}^{\prime\prime}]$ ) (e.g., Chakraborty et al., 1994; Fei et al., 2012). Accordingly, this has also been considered the case for hydrous olivine (e.g., Fei et al., 2013, 2018). However, by incorporation of 100 wt. ppm water ( $\text{H}/10^6\text{Si} \approx 1,600$ )

into olivine, which is the typical water content of the upper mantle (e.g., Workman & Hart, 2005), the  $[(4H)_{Si^{\times}}]/[Si_{Si^{\times}}]$  will be  $\sim 4 \times 10^{-4}$  if all protons form  $(4H)_{Si^{\times}}$ . In contrast,  $[V_{Mg}^{\prime\prime}]/[Mg_{Mg^{\times}}]$  is  $\sim 4 \times 10^{-5}$  in olivine (Tsai & Dieckmann, 2002). The major cation defects in hydrous olivine will therefore be hydrated  $V_{Si}$ , rather than Mg defects under asthenosphere conditions as considered previously (Kohlstedt & Mackwell, 1998; Mackwell & Kohlstedt, 1990; Wang et al., 2004).

#### 4.4. $C_{H_2O}$ Dependence of Atomic Diffusivity

We previously reported small  $C_{H_2O}$  exponents (0.2–0.3) for Si self-diffusion and larger values for Mg self-diffusivity ( $\sim 1.2$ ) in olivine (Fei et al., 2013, 2018). We argued that these observations are consistent with a predominant incorporation of protons in Mg sites (Fei et al., 2016, 2018). This is, however, not found to be the case in the present study. A new explanation therefore is necessary. The Si self-diffusion process can be expressed as  $Si_{Si^{\times}}(\text{site 1}) + V_{Si}(\text{site 2}) = V_{Si}(\text{site 1}) + Si_{Si^{\times}}(\text{site 2})$ , where  $V_{Si}$  is a defect on a Si site (either hydrated or unhydrated). This requires the breaking of four Si–O bonds by thermal activation. Although  $[V_{Si}]$  significantly increases by hydration, Si ions are very immobile owing to the high valence; thus, the diffusion process remains difficult, which leads to extremely slow Si self-diffusivity even though  $[V_{Si}]$  is high.

We consider that Si diffusion is dominated by  $V_{Si}^{\prime\prime\prime} \leftrightarrow Si_{Si^{\times}}$  exchange rather than  $Si_{Si^{\times}} \leftrightarrow (4H)_{Si^{\times}}$  because the later requires additional energy for breaking of O–H bonds. Under the charge neutrality condition of  $[(OH)_O^{\cdot}] = 4[V_{Si}^{\prime\prime\prime}]$ , we have  $[V_{Si}^{\prime\prime\prime}] \propto (f_{H_2O})^{2/5}$  and  $C_{H_2O} \propto (f_{H_2O})^2$  (Table 2), thus,  $[V_{Si}^{\prime\prime\prime}] \propto C_{H_2O}^{0.2}$ , which explains the small effect of water on Si self-diffusivity (Fei et al., 2013, 2018).

In the case of Mg diffusion, even though  $(2H)_{Mg^{\times}}$  is not the major species for protons, its concentration should still largely increase by proton incorporation, i.e.,  $[(2H)_{Mg^{\times}}]$  always increases linearly with increasing  $C_{H_2O}$  (Table 2). On the other hand, the activation energy for Mg diffusion is greatly reduced by water incorporation (Fei et al., 2018). This suggests enhanced probability of exchange (mobility) between  $V_{Mg}^{\prime\prime}$ ,  $(2H)_{Mg^{\times}}$ , and  $Mg_{Mg^{\times}}$ . As a result, the Mg self-diffusion coefficient increases significantly with increasing  $C_{H_2O}$  as reported from experiments (Fei et al., 2018).

Note that extremely fast proton diffusion in comparison with Si (e.g., Demouchy & Mackwell, 2003, 2006; Mackwell & Kohlstedt, 1990) is not inconsistent with the Si site incorporation mechanism. In spite of the immobile  $Si_{Si^{\times}}$ , protons could easily migrate from one  $V_{Si}$  or  $V_{Mg}$  defect to another without breaking Si–O or Mg–O bonds, i.e., exchange among defects of  $V_{Si}^{\prime\prime\prime}$ ,  $H_{Si}^{\prime\prime\prime}$ ,  $(2H)_{Si^{\prime\prime}}$ ,  $(3H)_{Si^{\prime}}$ ,  $(4H)_{Si^{\times}}$ ,  $V_{Mg}^{\prime\prime}$ ,  $H_{Mg}^{\prime\prime}$ , and  $(2H)_{Mg^{\times}}$ , or even interstitial  $H_i$ . Proton diffusion is therefore fast.

#### 4.5. Water Related Upper Mantle Geophysical Anomalies

The asthenosphere in the Earth's interior, which allows smooth motion of tectonic plates, is associated with anomalously low viscosity, low seismic velocity, high seismic attenuation, and high electrical conductivity. The origin of these geophysical anomalies has been debated for decades; however, no definite conclusion has been obtained (e.g., Cline et al., 2018; Hirth & Kohlstedt, 2003; Karato, 1990; Karato & Jung, 1998; Yoshino et al., 2006). Owing to the critical role that water may play in controlling geodynamic processes in the upper mantle, previous studies have investigated the effect of water on the physical properties of olivine (e.g., deformation, fabric transition, electrical conductivity) and attempted to attribute the geophysical anomalies in the asthenosphere to olivine hydration (e.g., Jung & Karato, 2001; Mei & Kohlstedt, 2000; Yang, 2012). However, a large proportion of such studies were performed below 2 GPa, therefore, protons are significantly maintained by Mg sites judging from the strong infrared absorptions at 3,150–3,350  $\text{cm}^{-1}$  in their samples (e.g., Mei & Kohlstedt, 2000; Yang, 2012). They are thus inapplicable for the deep asthenosphere (typically  $>2.5$  GPa) owing to the change of dominant incorporation mechanisms from both Mg and Si contributed to Si site dominated because different hydrated defects behavior differently in controlling the physical properties of olivine.

At 3–4 GPa, corresponding to  $\sim 100$  km depth where the geophysical anomaly is observed, the water solubility of olivine is about 80–130 wt. ppm (Figure 7), which is insufficient for the free proton-controlled conduction mechanism to account for the high conductivity in the asthenosphere (Yoshino et al., 2006). On the other hand, 80–130 wt. ppm water has a negligible effect on both the rheology and elasticity of olivine

(Cline II et al., 2018; Fei et al., 2013). Olivine hydration therefore cannot be the major reason for lithosphere softening that allows smooth plate motion as previously thought.

#### Acknowledgments

We appreciate the help of Heinz Fischer for high-pressure cell assembly preparation, Raphael Njul for sample polishing, Detlef Krauß and Anke Potzel for EPMA analysis, and Anthony Withers for helpful discussion regarding infrared analyses. Comments from Joseph Smyth and an anonymous reviewer were helpful to improve the manuscript. This work is financially supported by the Deutsche Forschungsgemeinschaft (DFG) to T. Katsura (KA3434/3-2, KA3434/7-1, KA3434/8-1, KA3434/9-1, KA3434/11-1, KA3434/12-1) and the Bayerisches Geoinstitut visiting scientist program to H. Fei. The EPMA and FTIR data for this paper are available in Zenodo (DOI: 10.5281/zenodo.3605122).

#### References

- Angel, R. J., & Jackson, J. M. (2002). Elasticity and equation of state of orthoenstatite,  $\text{MgSiO}_3$ . *American Mineralogist*, *87*, 558–561.
- Bai, Q., & Kohlstedt, D. L. (1992). Substantial hydrogen solubility in olivine and implications for water storage in the mantle. *Nature*, *357*, 672–674.
- Balan, E., Blanchard, M., Lazzeri, M., & Ingrin, J. (2014). Contribution of interstitial OH groups to the incorporation water in forsterite. *Physics and Chemistry of Minerals*, *41*, 105–114.
- Balan, E., Ingrin, J., Delattre, S., Kovacs, I., & Blanchard, M. (2011). Theoretical infrared spectrum of OH-defects in forsterite. *European Journal of Mineralogy*, *23*, 285–292.
- Bali, E., Bolfan-Casanova, N., & Koga, K. T. (2008). Pressure and temperature dependence of H solubility in forsterite: An implication to water activity in the Earth interior. *Earth and Planetary Science Letters*, *268*, 354–363.
- Bell, D. R., Rossman, G. R., Maldener, J., Endisch, D., & Rauch, F. (2003). Hydroxide in olivine: A quantitative determination of the absolute amount and calibration of the IR spectrum. *Journal of Geophysical Research*, *108*, 2105. <https://doi.org/10.1029/2001JB000679>
- Beran, A., & Putnis, A. (1983). A model of the OH positions in olivine, derived from infrared-spectroscopic investigations. *Physics and Chemistry of Minerals*, *9*, 57–60.
- Berry, A. J., Hermann, J., O'Neill, H. S. C., & Foran, G. (2005). Fingerprinting the water site in mantle olivine. *Geology*, *33*, 869–872.
- Blanchard, M., Ingrin, J., Balan, E., Kovacs, I., & Withers, A. (2017). Effect of iron and trivalent cations on OH defects in olivine. *American Mineralogist*, *102*, 302–311.
- Brodholt, J. P., & Refson, K. (2000). An ab initio study of hydrogen in forsterite and a possible mechanism for hydrolytic weakening. *Journal of Geophysical Research*, *105*, 18,977–18,982.
- Chakraborty, S., Farver, J. R., Yund, R. A., & Rubie, D. C. (1994). Mg trace diffusion in synthetic forsterite and San Carlos olivine as a function of P, T, and  $f\text{O}_2$ . *Physics and Chemistry of Minerals*, *21*, 489–500.
- Cline, C. J. II, Faul, U. H., David, E. C., Berry, A. J., & Jackson, I. (2018). Redox-influenced seismic properties of upper mantle olivine. *Nature*, *555*, 355–358.
- Costa, F., & Chakraborty, S. (2008). The effect of water on Si and O diffusion rates in olivine and implications for transport properties and processes in the upper mantle. *Phys. Earth Planet. Int.*, *166*, 11–29.
- Crépeisson, C., Bureau, H., Blanchard, M., Ingrin, J., & Balan, E. (2014). Theoretical infrared spectrum of partially protonated cationic vacancies in forsterite. *European Journal of Mineralogy*, *26*, 203–210.
- Demouchy, S., Deloule, E., Frost, D. J., & Keppler, H. (2005). Pressure and temperature-dependence of water solubility in Fe-free wadsleyite. *American Mineralogist*, *90*, 1084–1091.
- Demouchy, S., & Mackwell, S. (2003). Water diffusion in synthetic iron-free forsterite. *Physics and Chemistry of Minerals*, *30*, 486–494.
- Demouchy, S., & Mackwell, S. (2006). Mechanisms of hydrogen incorporation and diffusion in iron-bearing olivine. *Physics and Chemistry of Minerals*, *33*, 347–355.
- Dorogokupets, P. I. (2010). P-V-T equations of state of MgO and thermodynamics. *Physics and Chemistry of Minerals*, *37*, 677–684.
- Fei, H., Hegoda, C., Yamazaki, D., Wiedenbeck, M., Yurimoto, H., Shcheka, S., & Katsura, T. (2012). High silicon self-diffusion coefficient in dry forsterite. *Earth and Planetary Science Letters*, *345*, 95–103.
- Fei, H., & Katsura, T. (2016). Si and O self-diffusion in hydrous forsterite and iron-bearing olivine from the perspective of defect chemistry. *Physics and Chemistry of Minerals*, *43*, 119–126.
- Fei, H., & Katsura, T. (2020). High water solubility of ringwoodite at mantle transition zone temperature. *Earth and Planetary Science Letters*, *115987*. <https://doi.org/10.1016/j.epsl.2019.115987>
- Fei, H., Koizumi, S., Sakamoto, N., Hashiguchi, M., Yurimoto, H., Marquardt, K., et al. (2018). Mg lattice diffusion in iron-free olivine and implications to conductivity anomaly in the oceanic asthenosphere. *Earth and Planetary Science Letters*, *484*, 204–212.
- Fei, H., Wiedenbeck, M., Yamazaki, D., & Katsura, T. (2013). Small effect of water on upper-mantle rheology based on silicon self-diffusion coefficients. *Nature*, *498*(7453), 213–215. <https://doi.org/10.1038/nature12193>
- Ferrot, A., & Bolfan-Casanova, N. (2012). Water storage capacity in olivine and pyroxene to 14 GPa: Implications for the water content of the Earth's upper mantle and nature of seismic discontinuities. *Earth and Planetary Science Letters*, *349*, 218–230.
- Finkelstein, G. J., Dera, P. K., Jahn, S., Oganov, A. R., Holl, C. M., Meng, Y., & Duffy, T. S. (2014). Phase transitions and equation of state of forsterite to 90 GPa from single-crystal X-ray diffraction and molecular modeling. *American Mineralogist*, *99*, 35–43.
- Grant, K. J., Brooker, R. A., Kohn, S. C., & Wood, B. J. (2007). The effect of oxygen fugacity on hydroxyl concentrations and speciation in olivine: Implications for water solubility in the upper mantle. *Earth and Planetary Science Letters*, *261*, 217–229.
- Grant, K. J., Kohn, S. C., & Brooker, R. A. (2007). The partitioning of water between olivine, orthopyroxene, and melt synthesized in the system albite-forsterite- $\text{H}_2\text{O}$ . *Earth and Planetary Science Letters*, *260*, 227–241.
- Hirth, G., & Kohlstedt, D. L. (2003). Rheology of the upper mantle and the mantle wedge: A view from the experimentalists. *Geophysical Monograph*, *138*, 83–105.
- Ingrin, J., Liu, J., Depecker, C., Kohn, S. C., Balan, E., & Grant, K. J. (2013). Low-temperature evolution of OH bands in synthetic forsterite, implication for the nature of H defects at high pressure. *Physics and Chemistry of Minerals*, *40*, 499–510.
- Jung, H., & Karato, S. (2001). Water-induced fabric transitions in olivine. *Science*, *293*(5534), 1460–1463. <https://doi.org/10.1126/science.1062235>
- Karato, S. I. (1990). The role of hydrogen in the electrical conductivity of the upper mantle. *Nature*, *347*, 272–273.
- Karato, S. I., & Jung, H. (1998). Water, partial melting and the origin of the seismic low velocity and high attenuation zone in the upper mantle. *Earth and Planetary Science Letters*, *157*, 193–207.
- Kohlstedt, D. L., Keppler, H., & Rubie, D. C. (1996). Solubility of water in the  $\alpha$ ,  $\beta$  and  $\gamma$  phases of  $(\text{Mg,Fe})_2\text{SiO}_4$ . *Contributions to Mineralogy and Petrology*, *123*, 345–357.
- Kohlstedt, D. L., & Mackwell, S. J. (1998). Diffusion of hydrogen and intrinsic point defects in olivine. *Zeitschrift für Physikalische Chemie*, *207*, 147–162.
- Lemaire, C., Kohn, S. C., & Brooker, R. A. (2004). The effect of silica activity on the incorporation mechanisms of water in synthetic forsterite: A polarised infrared spectroscopic study. *Contributions to Mineralogy and Petrology*, *147*, 48–57.

- Litasov, K. D., Ohtani, E., Kagi, H., Jacobsen, S. D., & Ghosh, S. (2007). Temperature dependence and mechanism of hydrogen incorporation in olivine at 12.5–14.0 GPa. *Geophysical Research Letters*, *34*, L16314. <https://doi.org/10.1029/2007GL030737>
- Mackwell, S. J., & Kohlstedt, D. L. (1990). Diffusion of hydrogen in olivine: Implications for water in the mantle. *Journal of Geophysical Research*, *95*, 5079–5088.
- Matveev, S., O'Neill, H. S. C., Ballhaus, C., Taylor, W. R., & Green, D. H. (2001). Effect of silica activity on OH<sup>-</sup> IR spectra of olivine: Implications for low-*a*SiO<sub>2</sub> mantle metasomatism. *Journal of Petrology*, *42*, 721–729.
- Mei, S., & Kohlstedt, D. L. (2000). Influence of water on plastic deformation of olivine aggregates 1. *Diffusion creep regime. J. Geophys. Res.*, *105*, 21,457–21,469.
- Miller, G. H., Rossman, G. R., & Harlow, G. E. (1987). The natural occurrence of hydroxide in olivine. *Physics and Chemistry of Minerals*, *14*, 461–472.
- Mosenfelder, J. L., Deligne, N. I., Asimow, P. D., & Rossman, G. R. (2006). Hydrogen incorporation in olivine from 2–12 GPa. *American Mineralogist*, *91*, 285–294.
- Ohtani, E., Mizobata, H., & Yurimoto, H. (2000). Stability of dense hydrous magnesium silicate phases in the system Mg<sub>2</sub>SiO<sub>4</sub>-H<sub>2</sub>O and MgSiO<sub>3</sub>-H<sub>2</sub>O at pressures up to 27 GPa. *Physics and Chemistry of Minerals*, *27*, 533–544.
- Padron-Navarta, J. A., & Hermann, J. (2017). A subsolidus olivine water solubility equation for the Earth's upper mantle. *Journal of Geophysical Research*, *122*, 9862–9880.
- Qin, T., Wentzcovitch, R. M., Umemoto, K., Hirschmann, M. M., & Kohlstedt, D. L. (2018). Ab initio study of water speciation in forsterite: Importance of the entropic effect. *American Mineralogist*, *103*, 692–699.
- Smyth, J. R., Frost, D. J., Nestola, F., Holl, C. M., & Bromiley, G. (2006). Olivine hydration in the deep upper mantle: Effects of temperature and silica activity. *Geophysical Research Letters*, *33*, L15301. <https://doi.org/10.1029/2006GL026194>
- Tenner, T. J., Hirschmann, M. M., & Humayun, M. (2012). The effect of H<sub>2</sub>O on partial melting of garnet peridotite at 3.5 GPa. *Geochemistry, Geophysics, Geosystems*, *13*, Q03016. <https://doi.org/10.1029/2011GC003942>
- Tsai, T. L., & Dieckmann, R. (2002). Variation of the oxygen content and point defects in olivines, (Fe<sub>x</sub>Mg<sub>1-x</sub>)<sub>2</sub>SiO<sub>4</sub>, 0.2 ≤ x ≤ 1.0. *Physics and Chemistry of Minerals*, *29*, 680–694.
- Umemoto, K., Wentzcovitch, R. M., Hirschmann, M. M., Kohlstedt, D. L., & Withers, A. C. (2011). A first-principles investigation of hydrous defects and IR frequencies in forsterite: The case for Si vacancies. *American Mineralogist*, *96*, 1475–1479.
- Verma, A. K., & Karki, B. B. (2009). Ab initio investigations of native and protonic point defects in Mg<sub>2</sub>SiO<sub>4</sub> polymorphs under high pressure. *Earth and Planetary Science Letters*, *285*, 140–149.
- Wang, Z., Hiraga, T., & Kohlstedt, D. L. (2004). Effect of H<sup>+</sup> on Fe-Mg interdiffusion in olivine, (Fe,Mg)<sub>2</sub>SiO<sub>4</sub>. *Applied Physics Letters*, *85*, 209–211.
- Withers, A. C., Bureau, H., Raepsaet, C., & Hirschmann, M. M. (2012). Calibration of infrared spectroscopy by elastic recoil detection analysis of H in synthetic olivine. *Chemical Geology*, *334*, 92–98.
- Withers, A. C., & Hirschmann, M. M. (2008). Influence of temperature, composition, silica activity, and oxygen fugacity on the H<sub>2</sub>O storage capacity of olivine at 8 GPa. *Contributions to Mineralogy and Petrology*, *156*, 595–605.
- Withers, A. C., Hirschmann, M. M., & Tenner, T. J. (2011). The effect of Fe on olivine H<sub>2</sub>O storage capacity: Consequences for H<sub>2</sub>O in the Martian mantle. *American Mineralogist*, *96*, 1039–1053.
- Workman, R. K., & Hart, S. R. (2005). Major and trace element composition of the depleted MORB mantle (DMM). *Earth and Planetary Science Letters*, *231*, 53–72.
- Xue, X., Kanzaki, M., Turner, D., & Lorocho, D. (2017). Hydrogen incorporation mechanisms in forsterite: New insights from 1H and 29Si NMR spectroscopy and first-principles calculation. *American Mineralogist*, *102*, 519–536.
- Yang, X. (2012). Orientation-related electrical conductivity of hydrous olivine, clinopyroxene and plagioclase and implications for the structure of the lower continental and uppermost mantle. *Earth and Planetary Science Letters*, *317*, 241–250.
- Yoshino, T., Matsuzaki, T., Yamashita, S., & Katsura, T. (2006). Hydrous olivine unable to account for conductivity anomaly at the top of the asthenosphere. *Nature*, *443*(7114), 973–976. <https://doi.org/10.1038/nature05223>
- Zhao, Y., Ginsberg, S. B., & Kohlstedt, D. L. (2004). Solubility of hydrogen in olivine: Dependence on temperature and iron content. *Contributions to Mineralogy and Petrology*, *147*, 155–161.